Applied Surface Science 585 (2022) 152465

Contents lists available at ScienceDirect

Applied Surface Science

journal homepage: www.elsevier.com/locate/apsusc

Full length article

Asymmetric $XMoSiN_2$ (X=S, Se, Te) monolayers as novel promising 2D materials for nanoelectronics and photovoltaics

R.T. Sibatov [a,b,c,*], R.M. Meftakhutdinov [c], A.I. Kochaev [c]

[a] Department of Theoretical Physics, Moscow Institute of Physics and Technology (MIPT), Russia
[b] Research Laboratory for Advanced Processes, Scientific-Manufacturing Complex "Technological Centre", Moscow, Russia
[c] Laboratory of Diffusion Processes, Ulyanovsk State University, Ulyanovsk, Russia

ARTICLE INFO

Keywords:
2D material
Nanoelectronics
Density functional theory
XMoSiN2
Photovoltaics

ABSTRACT

In this paper, we study asymmetric 2D materials $XMoSiN_2$ constructed and optimized from $MoSi_2N_4$ by deleting SiN from one side and replacing remaining N atoms from the same side with chalcogen X atoms (sulfur, selenium, or tellurium). The new structure is a hybrid of a transition metal dichalcogenide and a 2D material from the $MoSi_2N_4$ family. We justify the dynamical stability of novel 2D materials. High binding energy (> 7.5 eV/atom) is typical for the monolayers under study. Estimated built-in electric field (~ 1.3 – 2 eV/Å) can serve to separate effectively photogenerated charge carriers in the single monolayer. Demonstrated high mechanical strength (2D Young modulus $E \sim 300$ N/m, in-plane stress limit > 17 N/m), noticeable sensitivity of the electronic and optical properties to deformations of monolayers, and weak sensitivity to an external transverse electric field indicate that the proposed 2D materials are of great promise for applications in flexible opto- and nanoelectronics.

1. Introduction

Since the first exfoliation of graphene from graphite in 2004 [1], various two-dimensional (2D) materials continue to attract a growing interest [2,3]. In the past decade, significant progress has been made in studies of graphene-like nanomaterials, such as phosphorene [4], silicene [5–7], germanene [8–10], transition metal dichalcogenides [11,12], hexagonal boron nitride [13–15], and other 2D materials [16–21]. Atomic monolayers can be used to obtain a very wide class of artificial materials, the so-called van der Waals (vdW) heterostructures [22,23]. Weak vdW interactions hold monolayers together without severe constraints on lattice matching. The availability of a wide variety of layered materials with different electronic properties, and the unique ability to exfoliate and repackage layered materials into complex heterostructures opened up a new direction in materials science and device design [3,22,23].

Of particular interest are monolayers of transition metal dichalcogenides (TMDCs), which are 2D materials with chemical formula MX_2, where M is a transition metal (molybdenum, tungsten, niobium, vanadium, etc.) and X is a chalcogen (sulfur, selenium, tellurium, etc.). The Properties of TMDC monolayers differ significantly from the properties of semimetallic graphene. Monolayers MoS_2, WS_2, $MoSe_2$, WSe_2, $MoTe_2$ are direct-gap semiconductors and can be used in electronics as elements of diodes and transistors, and in optics as emitters and detectors. Remarkable phenomena have been observed in TMDCs, such as charge density waves, superconducting and topological phases (see review [11]).

After obtaining TMDC monolayers, a number of works proposed 2D analogs of transition metal nitrides (TMNs) [24,25]. Since 3D crystals of TMNs do not have a layered structure, the production of TMN monolayers of a large area is a serious challenge. Recently, two-dimensional material $MoSi_2N_4$ consisting of a MoN_2 monolayer located between two Si–N monolayers has been synthesized [26]. The TMN monolayer MoN_2Si_4 demonstrates high strength and resistance at ambient temperatures. The elastic constant of $MoSi_2N_4$ is three times higher than that of the MoS_2 monolayer, and the mobility of electrons and holes in $MoSi_2N_4$ is approximately 4 and 6 times higher than that of MoS_2. The high mobility of carriers coupled with high thermodynamic stability makes this 2D material promising for applications in nanoelectronic devices.

Konstantin Novoselov in highlight-review [3] notes that the proposed method for obtaining $MoSi_2N_4$ in [26] is a general concept of creating such 2D materials using appropriate elements for passivating high-energy surfaces of non-layered materials during the growth process. During growing non-layered molybdenum nitride by chemical vapor deposition, the authors of [26] introduced elemental silicon, which made it possible to grow centimeter-scale monolayer films of

* Corresponding author at: Department of Theoretical Physics, Moscow Institute of Physics and Technology (MIPT), Russia.
E-mail address: ren_sib@bk.ru (R.T. Sibatov).

https://doi.org/10.1016/j.apsusc.2022.152465
Received 13 October 2021; Received in revised form 24 December 2021; Accepted 6 January 2022
Available online 4 February 2022

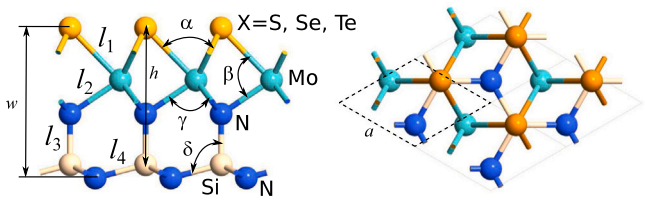

Fig. 1. The structure of $XMoSiN_2$ monolayer.

TMN $MoSi_2N_4$. Successful growth of another member from the family (WSi_2N_4 monolayer) using the same approach demonstrates versatility of the concept. Emphasizing the importance and generality of the method, K. Novoselov [3] unites new TMN monolayers into a whole family, the so-called $MoSi_2N_4$ family, marking the event of their synthesis on the history of 2D materials development.

Other materials of the family with formula MA_2Z_4 (M is a transition metal, A = Si, Ge and Z = N, P, As) were investigated using computational methods [27,28]. These monolayers are characterized by a wide range of properties from semiconductor to metallic. Some compounds with magnetic transition metal elements also have magnetic properties [29]. Monolayers $MoSi_2N_4$ and WSi_2N_4 exhibit high lattice thermal conductivity for thermoelectric applications [30]. The $MoSi_2N_4$ monolayer and some other MA_2Z_4 2D materials have a suitable band gap (up to 1.7 eV) for potential optical applications in the visible range [31,32].

In this work, to the best of our knowledge for the first time we propose the asymmetric 2D structures $XMoSiN_2$ obtained from $MoSi_2N_4$ by deleting SiN from one side and replacing remaining N atoms from the same side with chalcogen X atoms (sulfur, selenium, or tellurium). We investigate the properties of $XMoSiN_2$ monolayers using computational methods. The new 2D materials are asymmetric structures, hybrids of TMDCs and 2D material from the MA_2Z_4 family. The geometry of the structures under consideration is shown in Fig. 1. As is known, there are proposed many 2D materials, the so-called Janus type materials [17], with asymmetry relative to the atomic plane containing transition metal atoms. 2D Janus materials with different surfaces are attracting intense research interest due to their remarkable symmetry-breaking properties. One of the ways to fabricate a Janus material is substitutional doping of a 2D TMDC from the side of one layer. Apparently, the similar method is also applicable for obtaining $XMoSiN_2$ monolayers. The breaking of out-of-plane mirror symmetry by external electric fields makes it possible to obtain an additional way to manipulate the spin [33]. For the first time, the successful experimental synthesis of a 2D Janus-type TMDC has been reported in [34]. It is assumed that the new 2D structure should exhibit a strong splitting of the spin-polarized characteristics, which presumably can be controlled using a transverse electric field and/or applied mechanical stress. An intrinsic dipole in a 2D Janus TMDC can improve the spatial separation between photoexcited electrons and holes, preventing carrier recombination. Recently, various van der Waals heterostructures of TMDCs of the Janus type [35–37] have been studied.

The novel asymmetric monolayers proposed in this work and shown in Fig. 1 are characterized by a higher degree of asymmetry than the Janus TMDC structures. The built-in structural cross-plane asymmetry generates a dipole built into the $XMoSiN_2$ monolayer and this dipole can be stacked by putting the asymmetric $XMoSiN_2$ monolayers on top of each other by analogy with Janus TMDC layers [38]. It is important to establish the stability of the structures under consideration by analysis of calculated phonon band structures and elastic constants. Also, we study the electronic properties of $XMoSiN_2$ monolayers and consider the effect of deformations and external transverse electric fields on these properties.

2. Optimization and stability

The results are obtained using density functional theory (DFT) calculations implemented in the Quantum ATK package [39]. To optimize the initial structures and to relax materials under stress, we use the PseudoDojo pseudopotential [40] with a linear combination of basis sets of atomic orbitals (LCAO). The number of orbitals in the basis set is the same as in the double-zeta polarized set. The exchange correlation potential is described by the generalized gradient approximation (GGA) with Perdew–Burke–Ernzerhof (PBE) functional [41]. Optimization of the structures is carried out until the maximum force acting on each atom becomes less than 0.01 eV/Å, and the maximum change in energy between the two stages becomes less than 10^{-5} eV. The lattice cell is $a \times a \times 40$ Å, where a is a size of hexagonal unit cell. For optimized structures, values of a are given in Table 1. The k-point grids $15 \times 15 \times 1$ and $25 \times 25 \times 1$ of the Brillouin zone are used to optimize the structure and to calculate the electronic and optical properties. The density mesh cut-off is chosen equal to 240 Ry = 3265.37 eV for all calculations. The HSE06 hybrid exchange correlation functional is used to calculate the band structures, optical spectra and spin-polarized characteristics.

Fig. 1 shows the geometric structure of $XMoSiN_2$ (X = S, Se, Te) and its parameters. The corresponding values for optimized monolayers are given in Table 1.

To assess the stability of the structures under study, binding energies per atom are calculated according to the following formula (see e.g. [42])

$$E_b = \frac{E_{\text{total}} - E(\text{Mo}) - E(\text{Si}) - E(\text{X = S, Se, Te}) - 2E(\text{N})}{N}, \tag{1}$$

where E_{total} is the total energy of this cluster, E is the total energy of an isolated atom, N is the number of atoms in a unit cell. Quantity E_b determined in this way characterizes interatomic interactions, and it indicates the total energy required to separate the crystal into individual atoms.

The phase stability of the structures is determined from calculations of their formation energies E_{form} with respect to the most stable modifications of the elements constituting the compound:

$$E_{\text{form}} = \frac{E_{\text{total}} - E_t(\text{Mo}) - E_t(\text{Si}) - E_t(\text{X = S, Se, Te}) - 2E_t(\text{N})}{N}, \tag{2}$$

where E_{total} is the total energy of cluster, E_t are energies (per atom) calculated for optimized bulk structures Mo, α-Si, orthorhombic sulfur, γ-Se, α-Te and N_2 molecules.

In addition, as it was written above, the $XMoSiN_2$ structures are supposed to be obtained from MoN_2Si_4 by replacing SiN_2 on one side with chalcogen atoms X (sulfur, selenium or tellurium), so we calculated the energy E_{replace} required for such a replacement. This energy was calculated from considerations that first it is necessary to remove Si atom and two N atoms from one side, which is equivalent to the creation of three vacancies, and then to adsorb the chalcogen atom. So E_{replace} is defined as

$$E_{\text{replace}} = E_{\text{total}}(XMoSiN_2) - E_{\text{total}}(MoN_2Si_4) + E_t(\text{Si}) + 2E_t(\text{N}) - E_t(\text{X = S, Se, Te}). \tag{3}$$

Calculation results for E_b, E_{form} and E_{replace} are presented in Table 2.

It can be seen that all three monolayers are characterized by high binding energies, comparable to those for graphene (−7.9 eV/atom [43]). $E_b(TeMoSiN_2) = -7.56$ eV/atom, $E_b(SeMoSiN_2) = -7.85$ eV/atom, and $E_b(SMoSiN_2) = -8.20$ eV/atom. The $SMoSiN_2$ monolayer has a binding energy that exceeds the corresponding value for graphene. The formation energy of all structures takes on negative values, which indicates their stability. In addition, the substitutional energy for this monolayer is the lowest, which means that less energy is needed for its synthesis than for other monolayers proposed in present paper.

Table 1
Geometric parameters of monolayers $XMoSiN_2$ (X = S, Se, Te).

	a, Å	l_1, Å	l_2, Å	l_3, Å	l_4, Å	h, Å	w, Å	α	β	γ	δ
$SMoSiN_2$	2.989	2.38	2.11	1.76	1.80	4.62	5.115	77.75°	78.80°	90.03°	105.97°
$SeMoSiN_2$	3.034	2.53	2.12	1.77	1.83	4.79	5.270	73.67°	80.44°	91.43°	105.20°
$TeMoSiN_2$	3.105	2.72	2.14	1.77	1.85	4.98	5.433	69.59°	81.74°	93.21°	104.16°

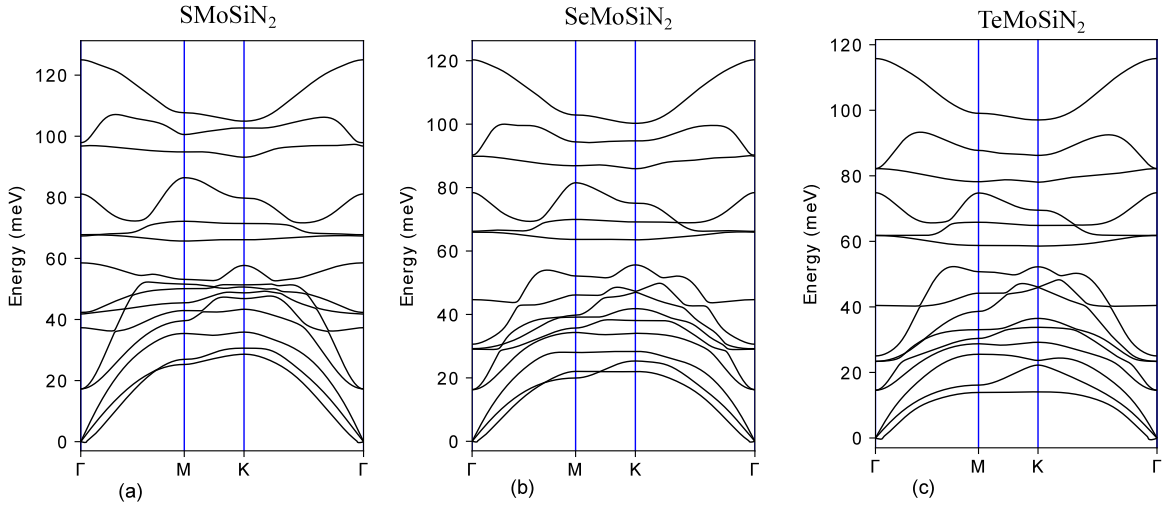

Fig. 2. Phonon band structures of the considered 2D materials.

Table 2
Energy characteristics of optimized structures $XMoSiN_2$ (X = S, Se, Te): binding E_b and formation E_{form} energies calculated per atom, and substitutional energy $E_{replace}$.

	E_b, eV/atom	E_{form}, eV/atom	$E_{replace}$, eV
$SMoSiN_2$	−8.20	−0.96	2.75
$SeMoSiN_2$	−7.85	−0.77	3.67
$TeMoSiN_2$	−7.56	−0.46	5.26

Table 3
Bandgap, SOC splitting of valence band Δ_V and conduction band Δ_C for monolayers $XMoSiN_2$ (X = S, Se, Te).

	E_g^{PBE}, eV	E_g^{HSE06}, eV	$E_g^{HSE06+SOC}$, eV	Δ_V, meV	Δ_C, meV
$SMoSiN_2$	2.15	2.67	2.58	171	18
$SeMoSiN_2$	1.73	2.40	2.26	0	30
$TeMoSiN_2$	1.02	1.58	1.54	0	51

Fig. 2 shows the phonon band structures of $XMoSiN_2$ monolayers. For each of them, 3 acoustic and 12 optical branches are found, corresponding to five atoms in a unit cell. The absence of negative branches of acoustic and optical phonons indicates the dynamic stability of isolated 2D layers. The long-wavelength region of phonon spectra of graphene [44], 2D MoS_2 [45], hybrid 2D materials [46] are characterized by the fact that acoustic longitudinal (LA) and transverse (TA) branches display linear dependence of vibration energy of in-plane phonons on the wavelength, whereas the acoustic out-of-plane (ZA) branch related vibrations of atoms in the direction perpendicular to the monolayer displays a quadratic dependence. In the case of the materials under consideration, Mo and N atoms (from the transition metal nitride) are trapped inside the entire structure through covalent bonds with the atoms on the surface that leads to less attenuation of transverse forces and to a change in the shape of the ZA branch in comparison with the known 2D materials, which becomes tougher. Earlier, similar behavior of this branch was found for a monolayer $MoTe_2$ upon imparting to it a biaxial tensile deformation [47]. Note that this phonon branch has a pronounced symmetric character. All presented phonon spectra contain three groups of branches separated by small forbidden gaps.

3. Electronic properties

In this section, we examine the electronic properties of $XMoSiN_2$ monolayers. Fig. 3 shows band structures calculated with PBE and HSE06 exchange–correlation functionals. The results show that $SMoSiN_2$ is a direct-gap semiconductor with the conduction band minimum (CBM) and the valence band maximum (VBM) located at the same point K. CBM and VBM of $SeMoSiN_2$ and $TeMoSiN_2$ monolayers lie at different points causing indirect band structures. In addition, for $SeMoSiN_2$, the location of CBM depends on the exchange functional used; for HSE06 it is located at K point and for PBE in the K → Γ valley. The bandgap values E_g are sensitive to the choice of calculation method (Table 3). The value of E_g^{PBE} is expected to be less than E_g^{HSE06}.

Although $XMoSiN_2$ is constructed from $MoSi_2N_4$, but there is an important difference in symmetries of these monolayers. The space group of $MoSi_2N_4$ is $P\bar{6}m2$, while the space group of $XMoSiN_2$ is $P3m1$. The absence of a horizontal plane of reflection in combination with the spin–orbit interaction due to the significant atomic weight of the transition metal can lead to band splitting due to the Rashba effect. Fig. 4 shows the projected band structures calculated taking into account the spin–orbit coupling (SOC). One can see that the interaction decreases the band gap, while maintaining the type of band structure (direct or indirect). In addition, for $SeMoSiN_2$ CBM SOC shifts from point K to valley K → Γ. Table 3 shows the values of the CBM and VBM splittings. In Fig. 4 one can find that for the $XMoSiN_2$ monolayer the electronic states near CBM and VBM are mainly associated with d-orbitals of the transition metal atom.

The CBM state of $SMoSiN_2$ consists of an out-of-plane Mo-d_{z^2} orbital, and the VBM state originates from the in-plane Mo-$d_{x^2-y^2}$ orbitals and Mo-d_{xy}. Strong hybridization between Mo-$d_{x^2-y^2}$ and Mo-d_{xy} orbitals results in a large SOC splitting of VBM at the K point.

For $SeMoSiN_2$ and $TeMoSiN_2$, CBM is located in the K → Γ valley and are associated with the orbitals Mo-d_{xy} + Mo-d_{yz} and Mo-d_{yz} + Mo-d_{z^2} respectively. The VBM of both structures is at the Γ point of high symmetry and is represented by the orbitals Mo-d_{z^2} and N-p_z, and the SOC splitting is not observed.

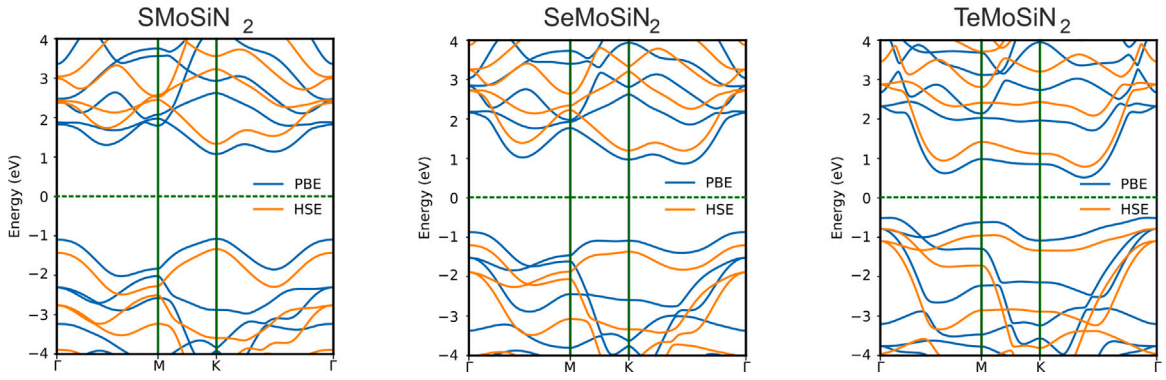

Fig. 3. $XMoSiN_2$ (X = S, Se, Te) band structures calculated with PBE and HSE06 functionals..

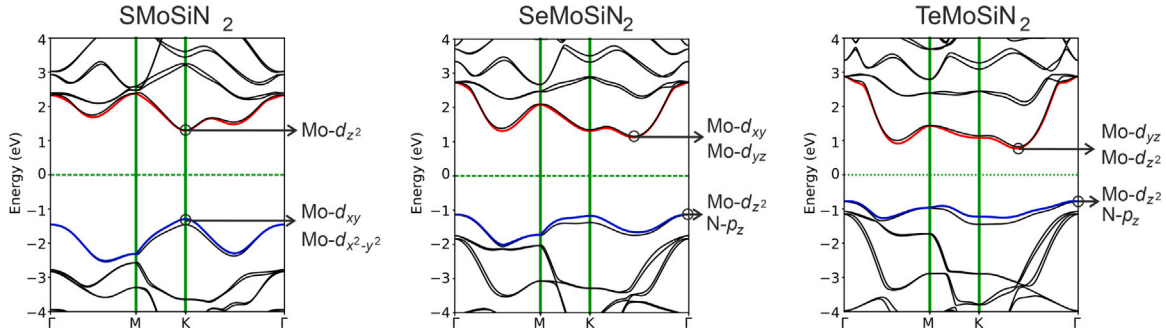

Fig. 4. Projected bandstructures $XMoSiN_2$ (X = S, Se, Te) calculated with HSE06+SOC functional.

Table 4
The lattice parameter, principal strain and bandgap for different values of stress in monolayers $XMoSiN_2$ (X = S, Se, Te).

$SMoSiN_2$	$\sigma = 0$ N/m	$\sigma = 3$ N/m	$\sigma = 6$ N/m	$\sigma = 12$ N/m	$\sigma = 24$ N/m
a, Å	2.989	3.014	3.042	3.105	3.291
ε, %	0	0.851	1.769	3.869	10.110
Direct bandgap, eV	2.650	2.514	2.375	2.086	1.455
Indirect bandgap, eV	2.650	2.452	2.237	1.790	0.839
$SeMoSiN_2$	$\sigma = 0$ N/m	$\sigma = 3$ N/m	$\sigma = 6$ N/m	$\sigma = 12$ N/m	$\sigma = 24$ N/m
a, Å	3034	3062	3091	3161	3401
ε, %	0	0.902	1.877	4.170	12.070
Direct bandgap, eV	2.568	2.433	2.296	2.005	1.339
Indirect bandgap, eV	2.387	2.197	2.005	1.599	0.719
$TeMoSiN_2$	$\sigma = 0$ N/m	$\sigma = 3$ N/m	$\sigma = 6$ N/m	$\sigma = 12$ N/m	$\sigma = 18$ N/m
a, Å	3.105	3.135	3.173	3.252	3.373
ε, %	0	0.974	2.183	4.749	8.638
Direct bandgap, eV	2.032	2.064	2.104	1.850	1.505
Indirect bandgap, eV	1.580	1.563	1.551	1.250	0.878

Fig. 5 allows us to estimate the vertical polarization by plotting the electrostatic potential and the electron difference density along the Z axis. One can see that redistribution of electrons occurs in all three structures. Due to the large electronegativity value (η = 3.04), the central nitrogen atom pulls electrons from the neighboring molybdenum and silicon atoms (electronegativity values are 2.16 and 1.9, respectively). From the side of Mo, the electron difference density Δn_e is larger than from the side of Si, because molybdenum has more electrons. The outer nitrogen atom also pulls electrons from silicon, but to a lesser extent than the central one. The electronegativity of external chalcogenes Se and S (η = 2.55 and 2.58, respectively) is slightly higher than the electronegativity of Mo; therefore, the maximum electron concentration is located at the interface between molybdenum and selenium or sulfur and is slightly shifted towards the latter, in contrast to Te (η = 2.10) where electrons are concentrated in the middle between the metal and chalcogen. Charge depletion is observed on the chalcogen atoms themselves. Due to the redistribution of electrons, local electric fields arise, one is directed from the outer nitrogen atom to the central one, while another is directed from the chalcogenide atom to the central nitrogen. Thus, a resulting field appears and it is directed from the chalcogen atom to the outer nitrogen. The highest intensity of this built-in field is for $TeMoSiN_2$ (2.03 VÅ^{-1}). For $SeMoSiN_2$, it is equal to 1.94 VÅ^{-1}, and for $SMoSiN_2$, to −1.29 VÅ^{-1}. This indicates a stronger vertical polarization of the $TeMoSiN_2$ monolayer. A positive charge at the structure boundary (Se, S, and Te atoms) facilitates the escape of electrons, which leads to a decrease in the work function and electrostatic potential gradients of 2.01 eV, 1.61 eV, and 0.47 eV for $TeMoSiN_2$, $SeMoSiN_2$ and $SMoSiN_2$, respectively.

Fig. 6 shows the dependence of deformations on stress for monolayers $XMoSiN_2$ (X = S, Se, Te). There is a deviation from the linear Hooke's law at deformations of more than 2 %. Due to the lower 2D Young modulus for the $TeMoSiN_2$ monolayer, it deforms more easily than $SMoSiN_2$ and $SeMoSiN_2$, and at mechanical stress > 20 N/m the $TeMoSiN_2$ monolayer, as shown by the numerical optimization of the

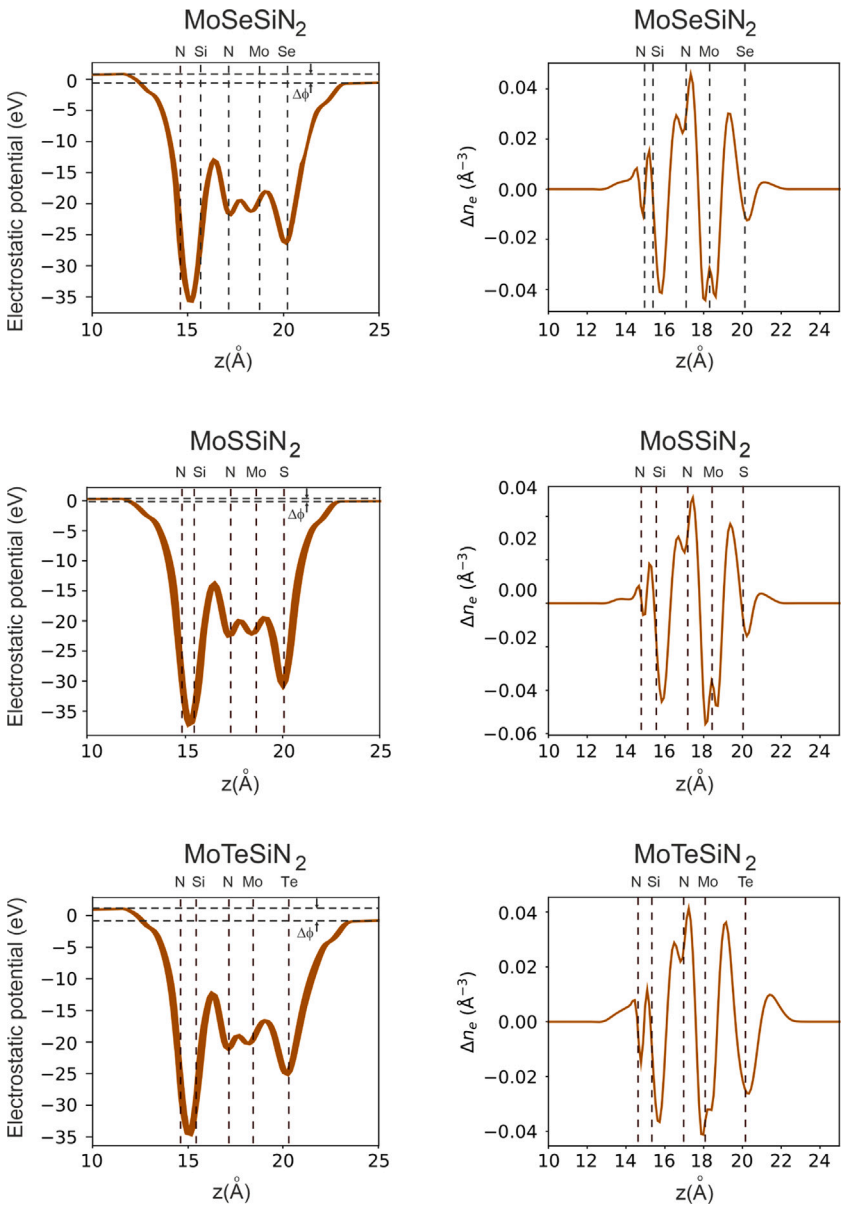

Fig. 5. Electrostatic potential and electron density difference in monolayers $XMoSiN_2$ (X = S, Se, Te).

stressed monolayer, collapses. The $SMoSiN_2$ monolayer has a larger value of 2D Young modulus than $SeMoSiN_2$. A similar relationship between the elastic constants is consistent with the sequence of bond lengths l_1 between chalcogen and transition metal atoms Mo (Table 1). The bandgap values for strained monolayers $XMoSiN_2$ (X = S, Se, Te) are given in Table 4 and Fig. 7.

Table 5 shows the bandgap values for different values of external transverse electric field strength $\mathcal{E}$. Despite the noticeable asymmetry of the electron density distribution and the substantial thickness of the monolayers > 4.5 Å, the bandgaps of the 2D materials under study are weakly dependent on the transverse field strength. The considered values of external electric fields are quite high but due to much higher built-in internal field the external one slightly perturbs electronic states.

Due to a remarkable deformation-induced change in the electronic properties of monolayers under study, the mechanical stress can also be used to control the optical properties.

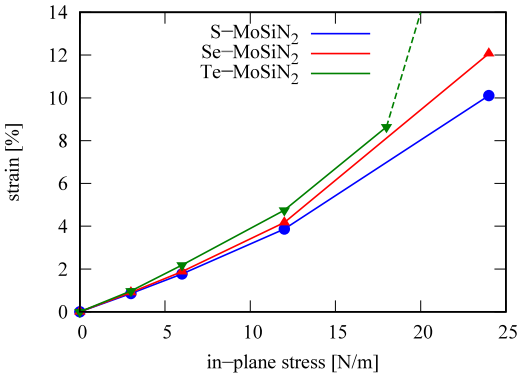

Fig. 6. Dependence of strain on stress for a monolayer $XMoSiN_2$ (X = S, Se, Te).

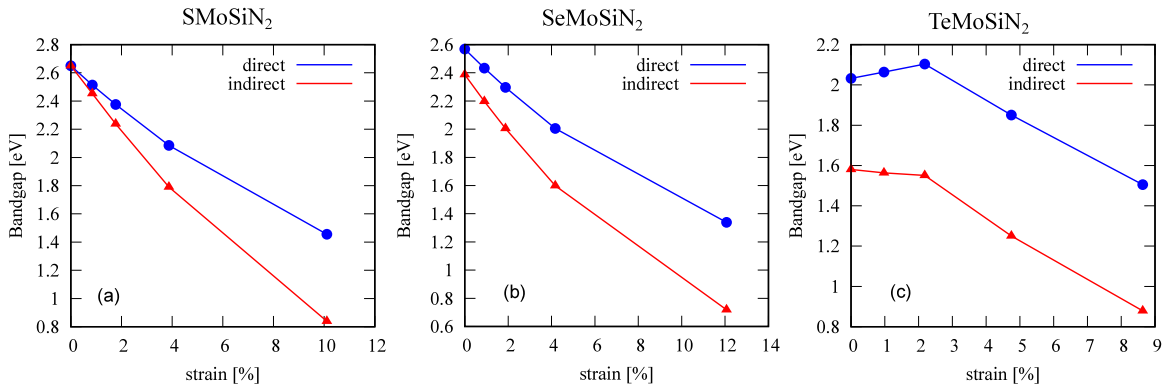

Fig. 7. Bandgap of the $XMoSiN_2$ (X = S, Se, Te) monolayer as a function of deformation ϵ.

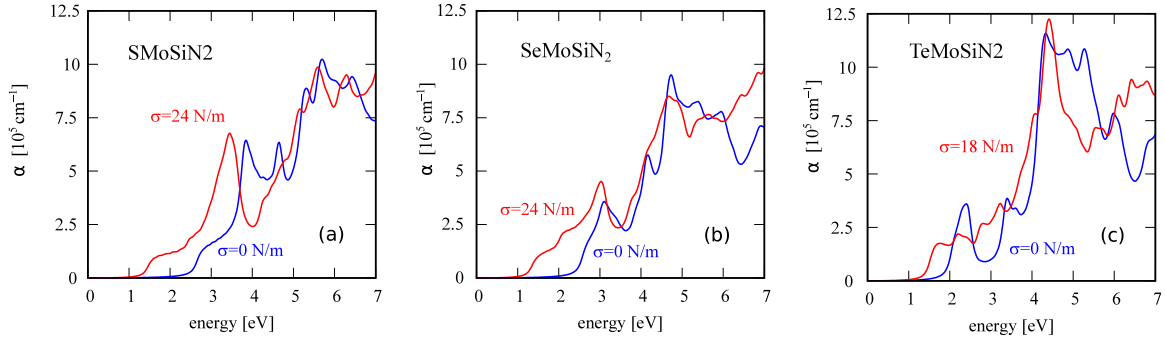

Fig. 8. Absorption spectra of free (blue line) and deformed under indicated stress (red line) monolayer $XMoSiN_2$ (X = S (a), Se (b), Te (c)).

Table 5
Bandgap of $XMoSiN_2$ (X = S, Se, Te) for different values of the transverse electric field strength.

$\mathcal{E}$, V/Å	−0.6	−0.45	−0.3	−0.15	0	0.15	0.3	0.45	0.6
$SMoSiN_2$	2.673	2.673	2.672	2.672	2.670	2.670	2.670	2.669	2.668
$SeMoSiN_2$	2.48	2.46	2.44	2.42	2.40	2.38	2.35	2.32	2.29
$TeMoSiN_2$	1.69	1.66	1.63	1.61	1.58	1.55	1.52	1.49	1.47

Table 6
Elastic constants, 2D Young modulus E, Poisson ratio ν.

	C_{11}, N/m	C_{12}, N/m	C_{66}, N/m	E, N/m	ν
$SMoSiN_2$	326.59	77.11	124.81	308.38	0.236
$SeMoSiN_2$	317.38	69.30	124.15	302.23	0.218
$TeMoSiN_2$	295.23	59.61	118.34	283.19	0.202
MoS_2 [48]	128.40	32.60	–	120.10	0.254
graphene [49]	352.00	62.60	–	340.80	0.178

To study the absorption spectra, the frequency-dependent complex dielectric function is calculated

$$\epsilon_r(\omega) = 1 + \chi(\omega), \tag{4}$$

where ω is the photon frequency. The dielectric susceptibility $\chi(\omega)$ is calculated within the framework of the Kubo–Greenwood formalism implemented in the QuantumATK package:

$$\chi_{ij}(\omega) = -\frac{e^2\hbar^4}{m^2\epsilon_0 V\omega^2}\sum_{nm}\frac{f(E_m)-f(E_n)}{E_{nm}-\hbar\omega-i\Gamma}\pi^i_{nm}\pi^j_{mn}, \tag{5}$$

where V is volume, f is the Fermi–Dirac function, $\Gamma = 0.1$ eV is the broadening, π^i_{nm} is the ith dipole matrix element between the states n and m. Local field effects are not included in the calculated permitivities and absorption spectra. The absorption coefficient is determined by the real part ϵ_1 and the imaginary part ϵ_2 of the dielectric function and is calculated by formula

$$\alpha(\omega) = \sqrt{2}\frac{\omega}{c}\left(\sqrt{\epsilon_1^2(\omega)+\epsilon_2^2(\omega)}-\epsilon_1^2(\omega)\right)^{1/2}. \tag{6}$$

Fig. 8 shows the absorption spectra (trace of tensor $\alpha_{ij}(E)$) for free and strained monolayers. One can see that the absorption edge can be significantly shifted due to a decrease in the bandgap upon stretching of monolayers. The absorption peaks become pronounced at photon energy of 3.4 eV for $SMoSiN_2$, 3.0 eV for $SeMoSiN_2$, and 4.4 eV for $TeMoSiN_2$.

Large values of the built-in electric field in the proposed structures indicate their applicability for stacked Janus-type solar-cell devices. Recently, in [38], it has been shown that an extremely thin (0.5–1 nm) device based on the Janus TMDC MoSSe generates a larger photocurrent and external quantum efficiency than 20–40 times thicker silicon-based devices. The proposed monolayers are characterized by higher values of built-in dipole moments.

Table 6 summarizes the elastic constants of $XMoSiN_2$ monolayers. For comparison, the values for graphene and MoS_2 are also provided. The Young modulus of $XMoSiN_2$ is similar to graphene's value, and 2.5 times higher than E of 2D molybdenite. Poisson ratio of $XMoSiN_2$ is close to TMDs parameter. High mechanical strength, stability, the demonstrated sensitivity of the electronic and optical properties to deformations of monolayers indicate that the considered 2D materials are promising for flexible nano- and optoelectronics.

4. Conclusion

The recently proposed and implemented method of synthesis of $MoSi_2N_4$ monolayer opens up new prospects for elaboration of the whole family of stable 2D materials for which there are no natural layered 3D crystals. High carrier mobility in monolayers, their stability under normal conditions make new 2D materials from the $MoSi_2N_4$ family promising for applications in nanoelectronics. In this work,

we proposed and investigated the asymmetric structures $XMoSiN_2$, constructed and optimized from $MoSi_2N_4$ by replacing SiN_2 on one side with chalcogen atoms (sulfur, selenium, or tellurium).

The new structure is a hybrid of a transition metal dichalcogenide and a 2D material from the $MoSi_2N_4$ family. The stability of new materials has been substantiated by means of DFT-based calculations. The monolayers under study are characterized by high values of the binding energy > 7.5 eV/atom.

In all studied monolayers, large built-in transverse electric field arises due to the redistribution of electrons enabling separation of the generated electron–hole pairs within one layer that is promising for photovoltaic applications.

The bandgaps of $XMoSiN_2$ monolayers are weakly dependent on the external transverse field strength $\mathcal{E}$ for the selected range of $\mathcal{E} \in [-0.6, 0.6]$ in V/Å. The considered values of external electric fields are quite high but due to much higher built-in internal field the external one slightly perturbs the electronic states.

The 2D Young modulus of $XMoSiN_2$ is similar to graphene's value, and 2.5 times higher than E of 2D molybdenite. The Poisson ratio of XMoSiN2 is close to the TMDCs parameter. The demonstrated sensitivity of the electronic and optical properties to deformations of monolayers, high mechanical strength and their stability indicate that the material is promising for stretchable opto- and nanoelectronics.

CRediT authorship contribution statement

R.T. Sibatov: Conceptualization, Methodology, Software, Reviewing and editing. **R.M. Meftakhutdinov:** Data curation, Writing – original draft. **A.I. Kochaev:** Visualization, Investigation, Software, Validation.

Declaration of competing interest

The authors declare that they have no known competing financial interests or personal relationships that could have appeared to influence the work reported in this paper.

Acknowledgment

This work was supported by the Ministry of Science and Higher Education of the Russian Federation (project # 075-15-2021-581).

References

[1] K.S. Novoselov, Electric field effect in atomically thin carbon films, Science 306 (5696) (2004) 666–669.
[2] A. Gupta, T. Sakthivel, S. Seal, Recent development in 2D materials beyond graphene, Prog. Mater. Sci. 73 (2015) 44–126.
[3] K.S. Novoselov, Discovery of 2D van der Waals layered MoSi2N4 family, Natl. Sci. Rev. 7 (12) (2020) 1842–1844.
[4] A. Carvalho, M. Wang, Xi Zhu, A.S. Rodin, H. Su, A.H. Castro Neto, Phosphorene: From theory to applications, Nature Rev. Mater. 1 (11) (2016) 1–16.
[5] S. Cahangirov, M. Topsakal, E. Aktürk, H. Şahin, S. Ciraci, Two- and one-dimensional honeycomb structures of silicon and germanium, Phys. Rev. Lett. 102 (23) (2009).
[6] H. Liu, J. Gao, J. Zhao, Silicene on substrates: A way to preserve or tune its electronic properties, J. Phys. Chem. C 117 (20) (2013) 10353–10359.
[7] T.P. Kaloni, N. Singh, U. Schwingenschlögl, Prediction of a quantum anomalous hall state in co-decorated silicene, Phys. Rev. B 89 (3) (2014).
[8] Linfei Li, Shuang zan Lu, Jinbo Pan, Zhihui Qin, Yu qi. Wang, Yeliang Wang, Geng yu Cao, Shixuan Du, Hong-Jun Gao, Buckled germanene formation on pt(111), Adv. Mater. 26 (28) (2014) 4820–4824.
[9] M.E. Dávila, L. Xian, S. Cahangirov, A. Rubio, G. Le Lay, Germanene: A novel two-dimensional germanium allotrope akin to graphene and silicene, New J. Phys. 16 (9) (2014) 095002.
[10] Raad Chegel, Somayeh Behzad, Tunable electronic, optical, and thermal properties of two- dimensional germanene via an external electric field, Sci. Rep. 10 (1) (2020).
[11] S. Manzeli, D. Ovchinnikov, D. Pasquier, O.V. Yazyev, A. Kis, 2D transition metal dichalcogenides, Nature Rev. Mater. 2 (8) (2017) 1–15.
[12] A.H. Castro Neto, Charge density wave, superconductivity, and anomalous metallic behavior in 2D transition metal dichalcogenides, Phys. Rev. Lett. 86 (19) (2001) 4382.
[13] M. Hofmann, Y.C. Shin, Ya-Ping Hsieh, M.S. Dresselhaus, J. Kong, A facile tool for the characterization of two-dimensional materials grown by chemical vapor deposition, Nano Res. 5 (7) (2012) 504–511.
[14] Li Song, Lijie Ci, Hao Lu, Pavel B. Sorokin, Chuanhong Jin, Jie Ni, Alexander G. Kvashnin, Dmitry G. Kvashnin, Jun Lou, Boris I. Yakobson, Pulickel M. Ajayan, Large scale growth and characterization of atomic hexagonal boron nitride layers, Nano Lett. 10 (8) (2010) 3209–3215.
[15] Jia Zhang, Biying Tan, Xin Zhang, Feng Gao, Yunxia Hu, Lifeng Wang, Xiaoming Duan, Zhihua Yang, PingAn Hu, Atomically thin hexagonal boron nitride and its heterostructures, Adv. Mater. (2020) 2000769.
[16] S. Haastrup, M. Strange, M. Pandey, T. Deilmann, P.S. Schmidt, N.F. Hinsche, M.N. Gjerding, D. Torelli, P.M. Larsen, A.C. Riis-Jensen, J. Gath, The computational 2D materials database: High-throughput modeling and discovery of atomically thin crystals, 2D Mater. 5 (4) (2018) 042002.
[17] A.C. Riis-Jensen, T. Deilmann, T. Olsen, K.S. Thygesen, Classifying the electronic and optical properties of Janus monolayers, ACS Nano 13 (11) (2019) 13354–13364.
[18] D.D. Vo, T.V. Vu, S. Al-Qaisi, H.D. Tong, T.S. Le, C.V. Nguyen, H.V. Phuc, H.L. Luong, H.R. Jappor, M.M. Obeid, N.N. Hieu, Janus monolayer PtSSe under external electric field and strain: A first principles study on electronic structure and optical properties, Superlattices Microstruct. 147 (2020) 106683.
[19] A.O. Almayyali, H.O. Muhsen, M. Merdan, M.M. Obeid, H.R. Jappor, Two-dimensional ZnI_2 monolayer as a photocatalyst for water splitting and improvement its electronic and optical properties by strains, Physica E 126 (2021) 114487.
[20] M.J. Abdulameer, S.S. Abed Al-Abbas, H.R. Jappor, Tuning optical and electronic properties of 2D ZnI_2/CdS heterostructure by biaxial strains for optical nanodevices: A first-principles study, J. Appl. Phys. 129 (22) (2021) 225104.
[21] A. Bafekry, C. Stampfl, M. Faraji, M. Yagmurcukardes, M.M. Fadlallah, H.R. Jappor, M. Ghergherehchi, S.A. Feghhi, A Dirac-semimetal two-dimensional ben_4: Thickness-dependent electronic and optical properties, Appl. Phys. Lett. 118 (20) (2021) 203103.
[22] Yuan Liu, Nathan O. Weiss, Xidong Duan, Hung-Chieh Cheng, Yu Huang, Xiangfeng Duan, Van der Waals heterostructures and devices, Nature Rev. Mater. 1 (9) (2016) 1–17.
[23] K.S. Novoselov, O.A. Mishchenko, O.A. Carvalho, A.H. Castro Neto, 2D materials and van der Waals heterostructures, Science 353 (6298) (2016).
[24] Qinye Li, Lizhong He, Chenghua Sun, Xiwang Zhang, Computational study of MoN2 monolayer as electrochemical catalysts for nitrogen reduction, J. Phys. Chem. C 121 (49) (2017) 27563–27568.
[25] Yao Wang, Shan-Shan Wang, Yunhao Lu, Jianzhong Jiang, Shengyuan A. Yang, Strain-induced isostructural and magnetic phase transitions in monolayer MoN2, Nano Lett. 16 (7) (2016) 4576–4582.
[26] Yi-Lun Hong, Zhibo Liu, Lei Wang, Tianya Zhou, Wei Ma, Chuan Xu, Shun Feng, Long Chen, Mao-Lin Chen, Dong-Ming Sun, et al., Chemical vapor deposition of layered two-dimensional MoSi2N4 materials, Science 369 (6504) (2020) 670–674.
[27] Lei Wang, Yongpeng Shi, Mingfeng Liu, Ao Zhang, et al., Intercalated architecture of MA2Z4 family layered van der Waals materials with emerging topological, magnetic and superconducting properties. Nature Communications 12 (1) (2021) 1–10.
[28] Hongxia Zhong, Wenqi Xiong, Pengfei Lv, Jin Yu, Shengjun Yuan, Strain-induced semiconductor to metal transition in MA2Z4 bilayers (M = TiCr, Mo; A = Si; Z = N, P), Phys. Rev. B 103 (8) (2021) 085124.
[29] Md Akanda, Rakibul Karim, Roger K. Lake, Magnetic properties of NbSi2N4, VSi2N4, and VSi2P4 monolayers, 2021, arXiv preprint arXiv:2105.01857.
[30] Bowen Li, Jiazhong Geng, Haoqiang Ai, Youchao Kong, Haoyun Bai, Kin Ho Lo, Kar Wei Ng, Yoshiyuki Kawazoe, Hui Pan, Design of 2D materials – MSi2CxN4-x (M = Cr, Mo, and W; x = 1 and 2) – with tunable electronic and magnetic properties, Nanoscale 13 (17) (2021) 8038–8048.
[31] Bohayra Mortazavi, Brahmanandam. Javvaji, Fazel Shojaei, Timon Rabczuk, Alexander V. Shapeev, Xiaoying Zhuang, Exceptional piezoelectricity, high thermal conductivity and stiffness and promising photocatalysis in two-dimensional MoSi2N4 family confirmed by first-principles, Nano Energy 82 (2021) 105716.
[32] Jihai Yu, Jian Zhou, Xiangang Wan, Qingfang Li, High intrinsic lattice thermal conductivity in monolayer MoSi2N4, New J. Phys. 23 (3) (2021) 033005.
[33] Hongtao Yuan, Mohammad Saeed Bahramy, Kazuhiro Morimoto, Sanfeng Wu, Kentaro Nomura, Bohm-Jung Yang, Hidekazu Shimotani, Ryuji Suzuki, Minglin Toh, Christian Kloc, et al., Zeeman-type spin splitting controlled by an electric field, Nat. Phys. 9 (9) (2013) 563–569.
[34] Ang-Yu Lu, Hanyu Zhu, Jun Xiao, Chih-Piao Chuu, Yimo Han, Ming-Hui Chiu, Chia-Chin Cheng, Chih-Wen Yang, Kung-Hwa Wei, Yiming Yang, et al., Janus monolayers of transition metal dichalcogenides, Nature Nanotechnol. 12 (8) (2017) 744–749.
[35] M. Idrees, H.U. Din, Shafiq Ur Rehman, M. Shafiq, Yasir Saeed, H.D. Bui, Chuong V. Nguyen, Bin Amin, Electronic properties and enhanced photocatalytic performance of van der Waals heterostructures of ZnO and Janus transition metal dichalcogenides, Phys. Chem. Chem. Phys. 22 (18) (2020) 10351–10359.

[36] M. Idrees, H.U. Din, R. Ali, G. Rehman, T. Hussain, C.V. Nguyen, Iftikhar Ahmad, B. Amin, Optoelectronic and solar cell applications of Janus monolayers and their van der Waals heterostructures, Phys. Chem. Chem. Phys. 21 (34) (2019) 18612–18621.

[37] Shiqiang Yu, Wei Wei, Fengping Li, Baibiao Huang, Ying Dai, Electronic properties of janus MXY/graphene (M = Mo, W; X ≠ Y = S, Se) van der Waals structures: A first-principles study, Phys. Chem. Chem. Phys. 22 (44) (2020) 25675–25684.

[38] M. Palsgaard, T. Gunst, T. Markussen, K.S. Thygesen, M. Brandbyge, Stacked janus device concepts: Abrupt pn-junctions and cross-plane channels, Nano Lett. 18 (11) (2018) 7275–7281.

[39] Søren Smidstrup, Troels Markussen, Pieter Vancraeyveld, Jess Wellendorff, Julian Schneider, Tue Gunst, Brecht Verstichel, Daniele Stradi, Petr A. Khomyakov, Ulrik G. Vej-Hansen, Maeng-Eun Lee, Samuel T. Chill, Filip Rasmussen, Gabriele Penazzi, Fabiano Corsetti, Ari Ojanperä, Kristian Jensen, Mattias L.N. Palsgaard, Umberto Martinez, Anders Blom, Mads Brandbyge, Kurt Stokbro, QuantumATK: An integrated platform of electronic and atomic-scale modelling tools, J. Phys.: Condens. Matter 32 (1) (2019) 015901.

[40] M.J. van Setten, M. Giantomassi, E. Bousquet, M.J. Verstraete, D.R. Hamann, X. Gonze, G.-M. Rignanese, The PseudoDojo: Training and grading a 85 element optimized norm-conserving pseudopotential table, Comput. Phys. Comm. 226 (2018) 39–54.

[41] John P. Perdew, Kieron Burke, Matthias Ernzerhof, Generalized gradient approximation made simple, Phys. Rev. Lett. 77 (18) (1996) 3865–3868.

[42] A.I. Kochaev, Hypothetical planar and nanotubular crystalline structures with five interatomic bonds of Kepler nets type, AIP Adv. 7 (2) (2017) 025202.

[43] P. Koskinen, S. Malola, H. Häkkinen, Self-passivating edge reconstructions of graphene, Phys. Rev. Lett. 101 (11) (2008) 115502.

[44] Sanjeev K. Gupta, Himadri R. Soni, Prafulla K. Jha, Electronic and phonon bandstructures of pristine few layer and metal doped graphene using first principles calculations, AIP Adv. 3 (3) (2013) 032117.

[45] Hans Tornatzky, Roland Gillen, Hiroshi Uchiyama, Janina Maultzsch, Phonon dispersion in MoS_2, Phys. Rev. B 99 (14) (2019) 144309.

[46] Jingang Wang, Xijiao Mu, Xinxin Wang, Nan Wang, Fengcai Ma, Wenjie Liang, Mengtao Sun, The thermal and thermoelectric properties of in-plane c-BN hybrid structures and graphene/h-BN van der Waals heterostructures, Mater. Today Phys. 5 (2018) 29–57.

[47] Aamir Shafique, Young-Han Shin, Strain engineering of phonon thermal transport properties in monolayer 2h-MoTe2, Phys. Chem. Chem. Phys. 19 (47) (2017) 32072–32078.

[48] Qing Peng, Suvranu De, Outstanding mechanical properties of monolayer MoS_2 and its application in elastic energy storage, Phys. Chem. Chem. Phys. 15 (44) (2013) 19427–19437.

[49] Qing Peng, Chao Liang, Wei Ji, Suvranu De, A theoretical analysis of the effect of the hydrogenation of graphene to graphane on its mechanical properties, Phys. Chem. Chem. Phys. 15 (6) (2013) 2003–2011.